Impact of shallow sills on heat transport and stratification regimes in proglacial fjords

Weiyang Bao[1] and Carlos Moffat[1]

[1]School of Marine Science and Policy, University of Delaware, Newark, DE, USA

Correspondence: Weiyang Bao (wbao@udel.edu)

Abstract. The increased melting and rapid retreat of glaciers is a main contributor to sea level rise. In shallow-silled fjords common in Patagonia, Alaska, and other systems, these bathymetric features may act as the first-order control on the dynamics, constraining fjord-shelf exchange and thereby modulating glacial melting. However, we still lack a clear understanding of how circulation and associated heat transport in shallow-silled glacial fjords are modulated by fjord-glacier geometry and fjord-shelf properties. To address this, idealized numerical simulations are conducted using a coupled plume-ocean fjord model. The steady-state fjord exhibits strong mixing and vertical transport over the sill. Relatively colder water from the upper-layer outflow is refluxed into the deeper layer, cooling the incoming warm oceanic water and modifying water properties near the glacier front. Driven by a shallow sill, up to $\sim$70% of the outflow is refluxed downward and leads to $\sim$10% cooling of the inflow and the deep fjord. A range of sensitivity experiments indicate that sill depth, subglacial discharge, ambient fjord temperature and stratification are key parameters that modulate the heat transport to the glacier terminus. In particular, the relative depth of the fjord, the sill, and the terminal height of meltwater plume are used to characterize four circulation and heat transport regimes. The sill-driven reflux is found to result in a decrease of both deep fjord temperature and stratification, which have opposite effects on the glacial melt rate. These results underscore the importance of sill bathymetry and associated fjord processes in the variability of oceanic heat supply to melting glaciers.

1 Introduction

From 2000 to 2019, global glaciers have lost mass at a rate of $\sim$267 $Gt\,yr^{-1}$, which amounts to approximately twenty percent of the observed sea-level rise (Hugonnet et al., 2021). As a critical link between glaciers, ice sheets, and the large-scale ocean, glacial fjords and their dynamics modulate the retreat rates of glaciers and the offshore transport of freshwater discharge. Increased submarine melting of glaciers terminating in fjords is the main cause for glacier retreat, and the resulting freshwater is transformed by fjord processes before being released to the ocean (Straneo and Cenedese, 2015). Knowledge of fjord dynamics and processes is thus key to estimating glacier melt rates and for understanding the fate of the meltwater in the coastal ocean.

At the fjord scale, the circulation can be influenced by tides, local winds and other air-sea exchange processes, and interactions of buoyancy-driven and intermediary flows (Straneo and Cenedese, 2015). At the glacier front, buoyant plumes generated by subglacial discharge and/or submarine melting are a source of mass and freshwater for the system (e.g., Xu et al., 2013; Kimura et al., 2014). The resulting buoyancy-driven circulation results from this freshwater leaving the terminus and mixing

with ambient water, the latter being replaced by a deep inflow towards the fjord head. The intermediary circulation driven by variability outside the fjord, on the other hand, is an effective mechanism for the advection of shelf anomalies inside the fjord, is often stronger than the estuarine-like circulation, and likely has an impact on melting rates (Sciascia et al., 2014; Moffat, 2014; Jackson et al., 2014). However, our estimates of submarine melt rates are still highly uncertain because of limited observations

30 and model accuracy (Jackson et al., 2020).

A key control on the circulation of fjord systems is the presence of a shallow sill (Geyer and Cannon, 1982; Arneborg et al., 2004; Inall et al., 2004). While many studies have focused on large fjord systems with no deep or no sill (Sutherland et al., 2014; Bartholomaus et al., 2016; Rignot et al., 2016), shallow sills are common in fjords in Alaska, Patagonia, and Greenland where the widespread retreat of glaciers is impacting sea-level rise and the regional ecosystems (Mortensen et al., 2013; Motyka

35 et al., 2013; Moffat et al., 2018). In southeastern Greenland, Sutherland et al. (2014) investigated the circulation regimes of two major outlet glacial fjords and found the magnitudes of the estuarine and intermediary circulation are determined by the sill depth compared to the fjord depth, with shallower sills corresponding to weaker intermediary circulation. In-situ observations collected in front of the floating tongue of a Greenland glacier also indicate the interface height between warm oceanic inflow and colder overlying water above the sill modulates the temporal variability of ocean heat transport through hydraulic control,

40 with a higher interface enhancing the cavity overturning circulation and the heat supplied for glacier melting (Schaffer et al., 2020).

Numerical simulation studies have also emphasized the importance of geometric parameters in controlling fjord renewal and exchange. Idealized modeling with varying depths of subglacial discharge in sill fjords shows that the depth of the grounding line compared to the sill is a primary control on the plume-driven renewal of basin waters (Carroll et al., 2017). When the inflow

45 is deeper than the sill, it is the former that determines the depth of the exchange circulation. For subglacial discharge entering at the grounding line of a glacier with a sill shallower than the terminus, the exchange flow spans the entire water column (Carroll et al., 2017). Besides, Zhao et al. (2021) addressed geometric and forcing parameters that control the fjord-to-shelf overturning circulation by piecing together theories for transport across the continental shelf, the fjord mouth sill, and the fjord head. Their numerical experiments demonstrated sill depth as one of the first-order controllers on the overturning circulation

50 and a functional prediction between the controlling parameters and the overturning transport was developed. Most recently, a study in LeConte Bay, Alaska based on both numerical modeling and observations showed that the deep, incoming flow can be cooled significantly at the sill by mixing with the outgoing freshwater outflow, a process called reflux (Hager et al., 2022). All of these studies highlight that mass and heat exchange process in fjords with shallow sills are significantly different from their deep-silled counterparts.

55 We aim to understand how the dynamics of shallow-silled fjords modulate the heat exchange and transport towards marine-terminating glaciers. We use numerical simulations based on a coupled plume-ocean model to investigate the constraining effects of the sill on the transport of heat from the open ocean to the glacier terminus, considering a broad range of fjord and forcing characteristics. We also aim to extend the results of Hager et al. (2022) for LeConte Bay to understand the role of reflux when different sill depths and forcing conditions are considered. Because freshwater discharge and ocean conditions in these

60 systems often vary significantly in seasonal scales, we aim to understand the circulation in that or shorter time-scales. We set

up our simulations to examine, in particular, the role of varying the sill depth, stratification, and freshwater discharge on heat transport and submarine melt rates. Our model setup is introduced in section 2, followed by results in section 3, and discussion and conclusions in sections 4 and 5, respectively.

2 Methodology

2.1 Coupled Plume-Ocean Fjord Model

We use the Massachusetts Institute of Technology General Circulation Model (MITgcm) in a three-dimensional, hydrostatic configuration. MITgcm (Marshall et al., 1997) includes options to incorporate horizontal ice shelves and vertical ice faces, and has been used in several studies of ice-ocean interactions both beneath ice shelves and in glacial fjords (Losch, 2008; Xu et al., 2012). Since the fjord-scale model lacks the grid resolution to resolve non-hydrostatic plume dynamics at the ice front, a theoretical plume model (Morton et al., 1956) is embedded as an MITgcm module in order to parameterize vertical convection in a half-conical, point source vertical plume adjacent to the glacier terminus (Cowton et al., 2015). The submarine melt rate is calculated based on the plume temperature, salinity, and velocity, as well as the ice-ocean boundary layer temperature and salinity (Holland and Jenkins, 1999). In our simulations, the freshwater input from submarine melting is parameterized as a virtual salt flux, generating a very small ($< 1\%$) increase in the exchange-flow transport and negligible freshening and cooling of fjord waters compared to that from subglacial discharge.

The model uses a vertical glacier terminus grounded to the fjord bottom, where subglacial runoff is specified and ambient conditions from the ocean are passed to the plume module at each time step. The module implements the evolution of a plume for a given buoyancy forcing, stratification and geometry from an idealized plume theory (Morton et al., 1956). Simplified expressions for the plume properties can be derived following the assumption that the entrainment velocity is a fixed fraction of the vertical velocity in the plume. The plume radius, velocity, temperature, salinity and vertical extent are calculated, with the plume ascent terminating when it reaches neutral buoyancy (i.e., plume density is equal to the ambient density) or the fjord surface. Water, heat, and salt are then removed from MITgcm cells in those vertical layers where the plume is entraining, and put into the cell at the depth at which the plume is predicted to terminate (Cowton et al., 2015). The plume model is run at each timestep using the current conditions within the fjord, with a steady-state solution calculated and applied as boundary conditions to the coarser fjord domain. This coupled model has the advantage of permitting a relatively coarse spatial and temporal resolution to be used throughout the domain, greatly increasing computational efficiency.

We emphasize, however, that the dynamical response of the submerged glacier terminus to ocean forcing is complex. Studies have shown, for example, that the formation of cavities in the ice that can significantly change the rates of submarine melting, driving higher than predicted melting (Jackson et al., 2017). While that complexity is not well represented in our simplified melting model, the qualitative change in melting rates from simplified models is still a useful guide for understanding how the geometry of the fjord and the forcing conditions impact heat transport and the circulation of the fjord.

To investigate the response of fjord circulation and submarine melting to variations in forcing and fjord geometry, we set up the plume-ocean fjord model in a domain with one Gaussian-shaped sill near the mouth (Fig. 1). The sill has a fixed width
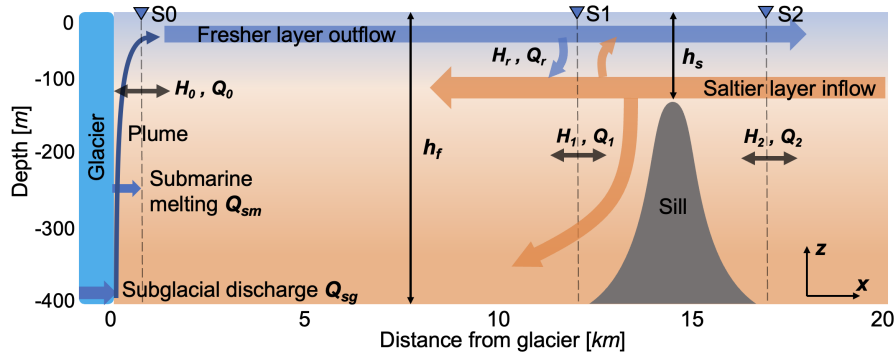
Figure 1. Two-dimensional (x, z) view of fjord domain and the plume-driven exchange flow. The maximum sill depth and fjord depth are denoted by h_s and h_f respectively, dashed lines represent cross-fjord sections near the glacier front (S0) and at the sill (S1, S2). H, Q are heat and volume fluxes through the sections and in the vertical (H_r, Q_r).

of 4 km and a maximum depth of h_s, which is varied in our simulations to examine the role of sill depth in modulating fjord

95 circulation and heat supply to the glacier. The fjord domain is set to 2 km to limit the scope of our study to a reasonable set of parameters. While relatively narrow, we will show that this not prevent the generation of significant cross-fjord variability in the circulation. The maximum depth of h_f is 400 m in all simulations. The fjord is 20 km long and opens to a shelf region (25 km wide and 400 m deep), with open boundaries at the north, south, and east edges. The cross-fjord grid resolution is 200 m inside the fjord, linearly increasing to 1 km at open boundaries. The along-fjord grid resolution ranges from 20 m at

100 the sill to 100 m at the rest of the fjord, also linearly telescoping to 1 km at open boundaries. Vertical grid size of the entire model domain increases from 2 m at the free surface to 6 m at the bottom.

Initial fjord conditions are horizontally homogeneous. Initial water temperature is a constant of 2 to 10 $°C$. The vertical salinity gradient is based on an idealized Greenland fjord profile (Cowton et al., 2015), where the salinity ranges from 32 to 33.8 at the surface and slowly increases to 34.5 at the bottom. To explore the impacts of fjord stratification, we also set

105 up a set of experiments with a simplified salinity profile linearly increasing from 23 at the surface to 27 with a stratification of 7.36×10^{-5} s^{-2} defined as $1N_0^2$. With a fixed mid-depth salinity, the gradient and thus the initial ambient stratification ranges from $0.5N_0^2$ to $4N_0^2$. Initial velocities are zero throughout the domain except for tidal simulations. For runs that include tidal forcing, this forcing is applied along the eastern boundary of the model domain in the form of a uniform zonal velocity $U_t = U_0 \sin(\frac{2\pi}{T} t)$ at the M2 tidal period (T=12.42 hr), the velocity amplitude U_0 is set to different values to generate weak

110 and strong tidal currents in the fjord relative to the non-tidal exchange flow. The Coriolis parameter is set to 1.2×10^{-4}. The nonlocal K-Profile Parameterization (KPP) scheme (Large et al., 1994) is used for vertical mixing. A quadratic bottom drag parameterization was used. The drag coefficient was 2.5×10^{-3} for most simulations, but we conducted a small set of simulations using a range $1\sim25 \times 10^{-3}$ to test the impact of varying bottom drag.

We also utilize passive tracers (MITgcm PTRACERS package) to estimate the timescales of the response of the fjord to

115 changes in shelf properties. For this purpose, a first tracer with a constant concentration of one was introduced at the entire

Table 1. List of fjord parameters and corresponding cases for simulations. h_s: maximum sill depth, h_f: maximum fjord depth, Q_{sg}: subglacial discharge, T_{ini}: initial fjord temperature, N_{ini}^2: initial fjord stratification, C_d: quadratic bottom friction coefficient, U_0: tidal amplitude at open boundary.

h_s/h_f	h (m)	$Q_{sg}\ (m^3\,s^{-1})$	T_{ini} (°C)	$N_{ini}^2\ (s^{-2})$	$C_d\ (\times 10^{-3})$	$U_0\ (cm\,s^{-1})$	# of Runs
0.04, 0.06, 0.08, 0.1, 0.12, 1	400	250	10	non-linear	2.5	0	6
0.04, 0.12, 1	400	25, 50, 100, 500, 1000	10	non-linear	2.5	0	15
0.04, 0.12, 1	200	25, 50, 100, 250, 500, 1000	10	non-linear	2.5	0	18
0.08	400	50, 500	2, 4, 6, 8	non-linear	2.5	0	8
0.04, 1	400	250	10	$0.5N_0^2, 1N_0^2, 2N_0^2, 3N_0^2, 4N_0^2$	2.5	0	10
0.04, 0.12	400	250	10	non-linear	1, 10, 25	0	6
0.04, 0.12	400	250	10	non-linear	2.5	0.01, 0.1, 0.5, 1, 6	10

shelf region, meanwhile a second tracer is injected into the same region with the same boundary conditions but its concentration increases with time at a fixed rate. Then the ratio of these two tracers in any model grid is used to estimate the "age" of the shelf water tracer at that location (e.g., Rayson et al., 2016; MacCready et al., 2021).

120   We analysed 73 model runs with a variety of parameters, including sill depth, subglacial discharge Q_{sg}, initial fjord temperature T_{ini}, stratification N_{ini}^2, bottom drag C_d and tidal forcing (Table 1). The maximum sill depth h_s is nondimensionalized by dividing by the fjord depth h_f, and this depth ratio h_s/h_f varies from 0.04 to 0.12 to characterize shallow-silled fjord systems e.g., in Alaska (Motyka et al., 2013; Love et al., 2016) and Patagonia (Moffat et al., 2018). Cases with no sill ($h_s/h_f = 1$) are included for reference. The subglacial discharge flux Q_{sg} is varied in the range 25 to 1000 $m^3\,s^{-1}$ to cover different magnitudes of freshwater forcing, and to represent the seasonal variation of runoff. All simulations are run for 60 days, in which the

125   fjord circulation reached a steady state for most cases.

2.2   Total Exchange Flow and Efflux-Reflux Calculations

The exchange flow along the fjord is calculated using the total exchange flow (TEF) method (MacCready, 2011). Transports through a cross-fjord section are sorted into salinity classes, tidally averaged and then integrated vertically and across the fjord. The inflow volume flux Q_{in} is the sum of the transport in all inward flowing salinity classes, and the flux-weighted salinity

130   of the inflow is S_{in}. Similarly, the outflow is quantified as Q_{out} and S_{out}. The TEF method decomposes salt flux in salinity space instead of physical space, yielding the exchange flow that incorporates both tidal and subtidal processes, and satisfies the Knudsen relation precisely (MacCready, 2011). TEF has been applied in many estuarine systems and has the ability to clearly characterize the exchange flow (Geyer and MacCready, 2014; Wang et al., 2017; MacCready et al., 2021). In our idealized fjord system presumably but not necessarily dominated by a two-layer circulation, using the TEF method gives the total inflow

135   and outflow fluxes through a cross-fjord section regardless of they are associated with exchange flow or tidal pumping.

     The volume transport through each cross-section is binned with salinity output stored every six hours, using 1000 bins between 0 and 35. After tidally averaging, the transport at each time is divided into inflowing and outflowing components
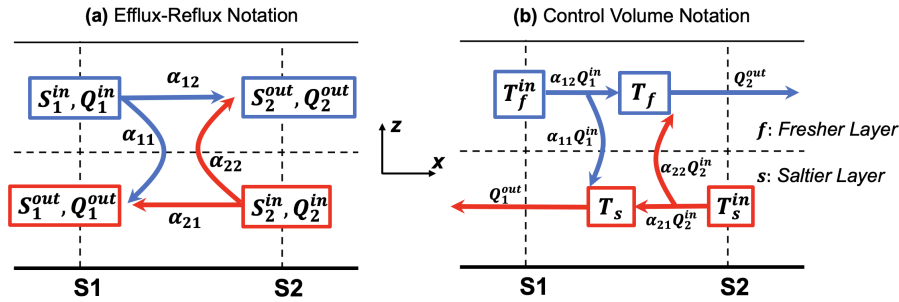
Figure 2. Notations of (a) efflux-reflux calculation and (b) a control volume. The segment in between sections S1 and S2 has a fresher layer and a saltier layer in the vertical. Temperature, salinity and volume fluxes are denoted by T, S and Q. $\alpha_{from,to}$ represent the efflux-reflux fractions. Figure modified from Fig. 7 in MacCready et al. (2021).

according to the "dividing salinity" method (MacCready et al., 2018). Integrating the transport in either landward or seaward components gives us Q_{in} and Q_{out}. Similarly, integrating the transport times the salinity of each bin in the two directions gives

140 the in- and outflow salt flux. Then S_{in} and S_{out} are derived from dividing the salt flux by volume flux in the same direction.

In order to estimate and quantify the vertical exchange between the upper and lower layers, we utilize the efflux-reflux formalism that was first developed in Cokelet and Stewart (1985) and has been applied to both estuary and glacial fjord studies (MacCready et al., 2021; Hager et al., 2022). In its simplest form, the efflux-reflux theory defines a channel segment between two cross-fjord sections. The segment consists of a steady two-layer exchange flow, with known salt and volume transports

145 through the cross-sections on either side (Fig. 2a). For the flow from any incoming layer, the reflux fraction corresponds to independent upward and downward turbulent transports across the segment, while efflux is the fraction that continues moving into the next reach. The reflux fraction thereby expresses the vertical fluxes as volume transports, which is equivalent to the horizontal fluxes in TEF. All transports are positive, the two cross-sections (S1 and S2) connect three segments, each of which has two layers in the vertical, a shallow fresher one and a deep saltier one. Following Cokelet and Stewart (1985), the system

150 of equations to be solved may be written as:

$$
\begin{bmatrix}
Q_2^{in} & Q_1^{in} & 0 & 0 \\
S_2^{in}Q_2^{in} & S_1^{in}Q_1^{in} & 0 & 0 \\
0 & 0 & Q_2^{in} & Q_1^{in} \\
0 & 0 & S_2^{in}Q_2^{in} & S_1^{in}Q_1^{in}
\end{bmatrix}
\begin{bmatrix}
\alpha_{22} \\
\alpha_{12} \\
\alpha_{21} \\
\alpha_{11}
\end{bmatrix}
=
\begin{bmatrix}
Q_2^{out} \\
S_2^{out}Q_2^{out} \\
Q_1^{out} \\
S_1^{in}Q_1^{in}
\end{bmatrix}
\tag{1}
$$

The efflux-reflux coefficients α are then determined by solving the matrix equation based on conservation of volume and salt, and the sum of efflux and reflux fractions should equal to unity, i.e., $\alpha_{11} + \alpha_{12} = \alpha_{21} + \alpha_{22} = 1$. In this framework, the vertical exchange components that we are primarily concerned with can be solved as:

155
$$\alpha_{11} = \frac{Q_1^{out}}{Q_1^{in}} \frac{S_2^{in} - S_1^{out}}{S_2^{in} - S_1^{in}}, \alpha_{22} = \frac{Q_2^{out}}{Q_2^{in}} \frac{S_2^{out} - S_1^{in}}{S_2^{in} - S_1^{in}} \tag{2}$$

Combining efflux-reflux fractions and TEF transports, a control volume can be defined for layer temperature along the fjord (Fig. 2b). It is also bounded by two cross-fjord sections S1 and S2, the free sea surface, sidewalls and the fjord bottom. The layer interface in the control volume is determined by the zero-crossing point of the along-channel velocity profile, an approximation of the exchange flow structure. Following the notation in Fig. 2b, the equation for the temperature of the lower

160 (saltier) layer with a volume of V_s can be expressed as:

$$\frac{\mathrm{d}T_s}{\mathrm{d}t} V_s = T_s^{in} Q_2^{in}(1 - \alpha_{22}) + T_f Q_1^{in} \alpha_{11} - T_s Q_1^{out} \tag{3}$$

At steady state ($\frac{\mathrm{d}T_s}{\mathrm{d}t} = 0$), the expression of the lower layer temperature becomes

$$T_s = \frac{T_s^{in} Q_2^{in}(1 - \alpha_{22}) + T_f Q_1^{in} \alpha_{11}}{Q_1^{out}} \tag{4}$$

As a result, we can use the reflux part (α_{11}, α_{22}) of the efflux-reflux calculation to determine the vertical transport in the
165 control volume. And to solve the matrix equation and obtain the efflux-reflux coefficients, we applied the TEF method at the cross-sections to get the salinity and transport (S and Q) of inflows and outflows. This approach quantifies the net effect of mixing and vertical exchange in the fjord without the need to resolve the process itself. To address the role of sill in modulating vertical transports and the heat supply to the glacier terminus, TEF transports, reflux coefficients and deep-layer temperature are estimated in the segment bonded by cross-fjord sections on either side of the sill (Fig. 1). Another cross-section is used to
170 calculate the volume and heat fluxes near the glacier front. These segments are also defined to construct the volume and heat budgets within the fjord, following the framework in a generic glacial fjord study by Jackson and Straneo (2016).

3 Results

3.1 Base Case: First-Order Impacts of a Shallow Sill

To illustrate the first-order impact of the sill on fjord-shelf exchange in our runs, we present a base case driven only by
175 subglacial discharge in fjords under varying sill depths. A buoyant plume is generated by the fresh and cold subglacial runoff that enters the fjord at the glacier grounding line, entraining ambient warm water while rising vertically along the glacier front. With a fixed discharge of 250 $m^3 s^{-1}$, the plume drives a thin and cold down-fjord current in the upper part of the water column, balanced by a thick and warm up-fjord current at depth, and the fjord reached a steady state after about a week. Runs with with varied sill-fjord depth ratios (i.e., h_s/h_f) ranging from 0.04 to 0.12 allowed to focus on the impact on shallow sills
180 on the exchange of mass and heat between the fjord and the shelf (Fig. 3).
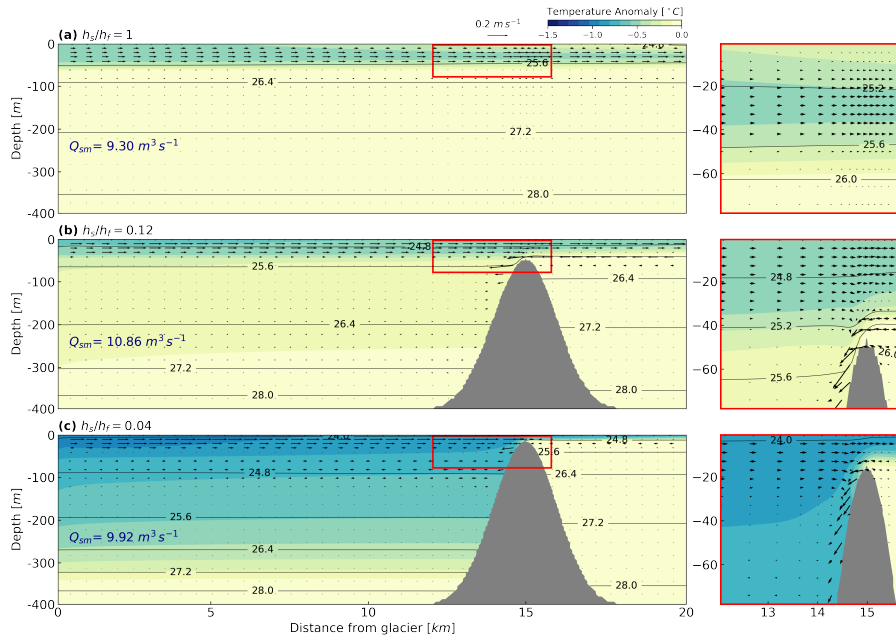
Figure 3. Time-mean potential temperature anomaly (with respect to initial temperature) along the fjord with $Q_{sg} = 250 \ m^3 \ s^{-1}$ and (a) $h_s/h_f = 1$, (b) $h_s/h_f = 0.12$, (c) $h_s/h_f = 0.04$. Red-outlined areas are zoomed in the right panels, with vertical velocity scaled up by a factor of 15. Black contours denote water density anomaly, Q_{sm} is average submarine melting of the glacier front.

As the sill depth increases, the layer thickness of the surface outflow initially remains between 40 to 45 m in the fjord interior, but eventually decreases after reaching the sill with sill-fjord depth ratios <0.12. In these shallow sill cases, the lower-layer inflow cools by 0.2 to 1 $°C$ as it moves from the shelf to the fjord interior. The cooling of the deep fjord water is most significant above ~350 m. Both the structure of the exchange flow and the temperature and density fields over the sill show that a frontal zone is formed near the sill crest (Fig. 3b, 3c). The front becomes steeper with smaller h_s/h_f as currents accelerate significantly down the slope after crossing the sill. Strong mixing is observed in this region and results in the upper-layer outflow recirculating before passing the sill, cooling the deep fjord as a result.

In order to examine the influence of sill depth on the volume and heat transport, we applied a simplified framework of heat and volume budgets for the fjord. A control volume is defined such that it is bounded by the cross-fjord section S0 near the glacier front, and by the cross-section S2 on the oceanward side of the sill (see Fig. 1). There's no heat exchange with the overlying atmosphere. The time-mean heat flux (H) and volume flux (Q) through the cross-section for two layers, and vertically through the layer interface are calculated (Table 2, Table 3), positive values represent fluxes in the down-fjord direction and negative values indicate fluxes that are transported in the up-fjord direction. The interface between the upper and lower layers was defined kinematically as the zero crossing of the along-fjord velocity profile. As expected, the heat budget of the control volume is dominated by advective processes, with much smaller diffusive heat fluxes (not shown here). Near the glacier front, both the advective heat flux (H_0^f, H_0^s) and the volume flux (Q_0^f, Q_0^s) slightly decrease with smaller h_s/h_f in most cases with a

Table 2. Time-mean advective heat flux (H) through the cross-fjord sections and in the vertical. Superscripts f, s, r represent fresher layer, saltier layer, and vertical direction respectively. Subscripts 0, 1, 2 denote the cross-fjord sections S0, S1, and S2.

h_s/h_f	H_0^f ($\times10^{11}Js^{-1}$)	H_0^s ($\times10^{11}Js^{-1}$)	H_1^f ($\times10^{11}Js^{-1}$)	$H1^s$ ($\times10^{11}Js^{-1}$)	H_2^f ($\times10^{11}Js^{-1}$)	H_2^s ($\times10^{11}Js^{-1}$)	H_r ($\times10^{11}Js^{-1}$)
0.04	2.51	-2.54	2.83	-2.85	0.87 [0.35]	-0.88	-2.05 [51]
0.06	2.78	-2.81	3.09	-3.12	1.32 [0.53]	-1.35	-1.94 [49]
0.08	2.96	-2.99	3.2	-3.24	1.69 [0.68]	-1.72	-1.60 [40]
0.10	3.05	-3.08	3.19	-3.22	2.00 [0.80]	-2.03	-1.36 [34]
0.12	2.88	-2.91	2.95	-2.99	2.22 [0.89]	-2.26	-0.73 [18]
1	2.38	-2.41	2.45	-2.48	2.49	-2.53	0.04

[ ]: the magnitude relative to the $h_s/h_f = 1$ case

Table 3. Time-mean volume flux (Q) through the cross-fjord sections and in the vertical. $f, s, r, 0, 1, 2$ are same as in Table 2, Q_{sm} is submarine melting flux.

h_s/h	Q_0^f (m^3s^{-1})	Q_0^s (m^3s^{-1})	Q_1^f (m^3s^{-1})	Q_1^s (m^3s^{-1})	Q_2^f (m^3s^{-1})	Q_2^s (m^3s^{-1})	Q_r (m^3s^{-1})	Q_{sm} (m^3s^{-1})
0.04	7154	-6904	8041	-7792	2447 [0.37]	-2199	-5647 [57]	9.92
0.06	7683	-7433	8514	-8264	3636 [0.55]	-3386	-5188 [52]	10.32
0.08	8026	-7776	8653	-8404	4571 [0.69]	-4323	-4215 [43]	10.36
0.10	8159	-7909	8507	-8257	5344 [0.81]	-5094	-3535 [36]	10.52
0.12	7658	-7408	7849	-7600	5911 [0.90]	-5662	-1899 [19]	10.86
1	6298	-6048	6466	-6216	6573	-6323	99	9.3

[ ]:the magnitude relative to the $h_s/h_f = 1$ case

shallow sill, indicating the fjord water is cooled with shallower sills. In contrast, the heat and volume fluxes close to the fjord mouth (H_2^f, H_2^s and Q_2^f, Q_2^s) are reduced significantly as the sill becomes shallower, adding more constrictions and colder water from the fjord head. Compared to the no-sill case ($h_s/h_f = 1$), the near-mouth exchange heat and volume fluxes in the shallowest-sill case ($h_s/h_f = 0.04$) is about 64% smaller.

The impact of the sill in the vertical heat and mass exchange at the sill are shown in Table 2 and 3. As expected, the volume and heat fluxes (H_r, Q_r, positive upwards) through the interface separating the upper and lower layers is near zero in the absence of a sill. As the sill becomes shallower, they become increasingly negative, i.e., shallower sills result in enhanced downward transport and cooling of the lower, warm water inflow. As h_s/h_f decreases from 0.12 to 0.04, the downward volume transport Q_r and the deeper layer heat loss H_r increases by a factor of ~3, with magnitudes comparable to the horizontal fluxes across the sill. In addition, fluxes at the glacierward side of the sill (H_1^f, H_1^s and Q_1^f, Q_1^s) are comparable with those near the glacier front, indicating that the vertical transport occurs mostly in between sections S1 and S2, and over the sill.
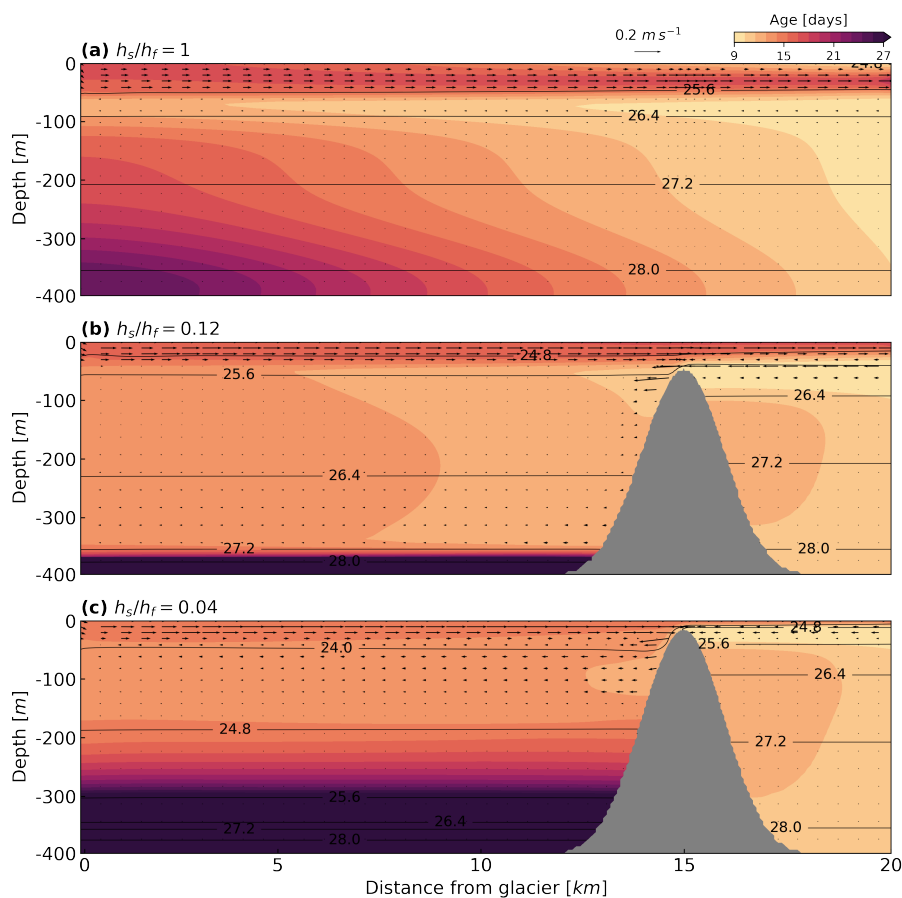
Figure 4. Along-fjord distribution of the shelf water tracer age at the end time of simulation. $Q_{sg} = 250\ m^3\,s^{-1}$, black contours denote water density anomaly.

The presence of the sill also impacts the response time-scale of the fjord to shelf variability (Fig. 4). In our experiments where the shelf water is set to an age of zero, the tracer age increases, as expected, with depth and distance from the shelf, and the shelf water takes less than 23 days to reach the entire fjord when no sill is present (Fig. 4a). As the sill becomes shallower and mixing near the sill increases, the maximum intrusion depth in the fjord is found to decrease as more of the lighter outflow is entrained into the inflowing oceanic water. Comparing the velocity and density profiles in Fig. 4b and 4c, the intrusion depth of shelf water decreases from about $350\ m$ to $250\ m$ as h_s/h_f reduces from 0.12 to 0.04. Consistent with the circulation pattern, the tracer is younger within the intruding water than the underneath layer, where the deep basin is progressively and slowly (>27 days) filled by waters at the sill depth.

The active mixing occurring at the sill can be examined using the Froude number around the sill. Layer-averaged along-fjord velocity and layer salinity are defined as U_{upper}, U_{lower} and S_{upper}, S_{lower} respectively. The Froude numbers are then
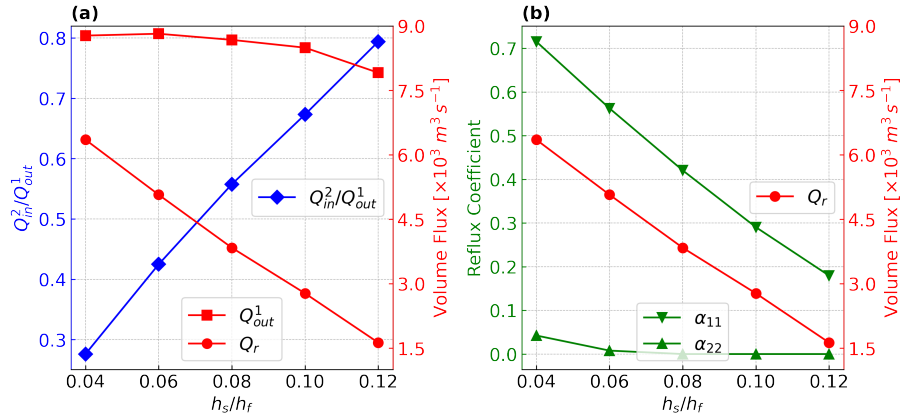
Figure 5. TEF transports (a) and reflux fractions (b) with varing sill depths. 1, 2 denote the cross-fjord section on either side of the sill; Q_{in}: volume flux of the water flowing into the fjord; Q_r: downward reflux; α_{11} and α_{22} correspond to downward and upward reflux fraction respectively.

determined as

$$Fr_{upper} = \frac{U_{upper}}{\sqrt{g'h_{upper}}}, Fr_{lower} = \frac{U_{lower}}{\sqrt{g'h_{lower}}} \qquad (5)$$

220   where $g' = g\frac{\rho_{lower} - \rho_{upper}}{\rho_{lower}}$ is the reduced gravity, ρ, h denote the upper- and lower-layer density and thickness.

Along the channel, the upper-layer outflow remains subcritical while the lower-layer Froude number changes dramatically over the sill as the inflow approaches to being supercritical with shallower sills (not shown). Specifically, as h_s/h_f goes below 0.06, the lower-layer Froude number Fr_{lower} exceeds one at the top of the sill, and an hydraulic jump is formed. With shallower and thus steeper sills, the lower-layer inflow experiences a greater acceleration down the sill, creating a strong velocity shear

225   at the interface with the upper outflow. The enhanced shear and hydraulic transition over the sill lead to conditions favorable for mixing and entrainment of the exchange flow, which are reflected in the enhanced downward flux of heat and mass shown earlier.

In order to quantify the entrainment to the sill overflow and to estimate the heat supply from the fjord to the glacier, we first calculated the TEF transports at cross-sections (S1 and S2) on both sides of the sill. The temporal average of the TEF

230   inflow and outflow volume flux was defined as Q_{in} and Q_{out}. Based on volume conservation at steady state, the entrainment flux (downward reflux) Q_r across the upper-bounding isohaline surface equals the divergence of inflow or outflow through the segment bonded by two cross-sections (Wang et al., 2017). In the sill segment we defined, the volume fluxes of the exchange flow and the entrainment under different sill depths are characterized using the TEF calculation (Fig. 5).

Changes in volume flow towards the fjord head from section S1 to S2 reveal the modulation of water transport by the sill.

235   With shallower sills, Q_{out}^1 remains almost unchanged while Q_{in}^2/Q_{out}^1 decreases by $\sim$0.5, showing that the water incoming transport (Q_{in}^2) is constrained by the sill. It also suggests other sources of water supply in the sill segment. Noticeably, the reflux over sill (Q_r) increases with smaller h_s/h_f and can reach about 70% of the inflow within the fjord (Q_{out}^1). This process
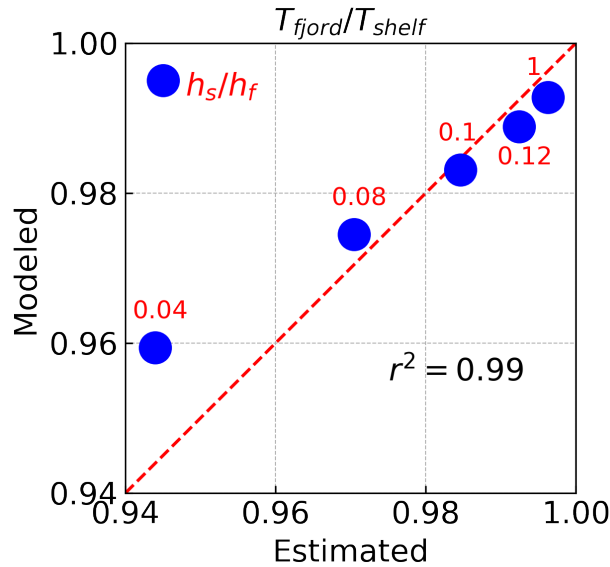
Figure 6. A comparison between the deep water temperature estimated from Eq. (4) and from the model. Fjord temperature is non-dimensionalized by shelf-water temperature. Increasing marker sizes correspond to increasing values of sill-fjord depth ratio h_s/h_f.

of reflux of the cold upper layer water into the warmer, lower layer largely compensates for the reduction of the exchange flow at the sill. That is, the exchange circulation in the fjord away from the sill does not weaken significantly, but rather the lower layer becomes colder.

Consistently with the above, the upward reflux coefficient α_{22} is close to zero in all these cases. As the sill becomes shallower, the downward fraction α_{11} increases nearly linearly and is consistent with the variation of reflux Q_r. As h_s/h_f decreases from 0.12 to 0.04, Q_r increases by about 5000 $m^3 s^{-1}$, and at least 50% more of the outflowing water is refluxed into the deep layer.

The estimated deep water cooling that results from the reflux process can be reasonably predicted using Eq. (4) (Fig. 6), where temperature is non-dimensionalized by T_s^{in}, and their ratio T_{fjord}/T_{shelf}, indicates the relative water temperature in the fjord compared to the shelf-water temperature. With a minor ($< 4\%$) adjustment to the downward reflux coefficient α_{11}, the theory predicts the deep water temperature with a coefficient of determination of $r^2 = 0.99$. Despite some discrepancies, both estimated and modeled results show that the deep fjord is $0.1 \sim 1\ °C$ colder than the shelf water depending on the sill depth. In the shallowest sill case ($h_s/h_f = 0.04$), the warm inflow from the shelf is cooled around 10% by the sill-driven reflux.

3.2 Circulation and Heat Transport Regimes

The base run discussed in Section 3.1 illustrates the case where the resulting fjord circulation closely resembles a typical shallow-silled fjord–i.e., with no marine-terminating glacier–where a two layer exchange flow is formed and strong control on the exchange is exerted by the sill. A key difference, however, is that adding a deep source of buoyancy at the head of the fjord
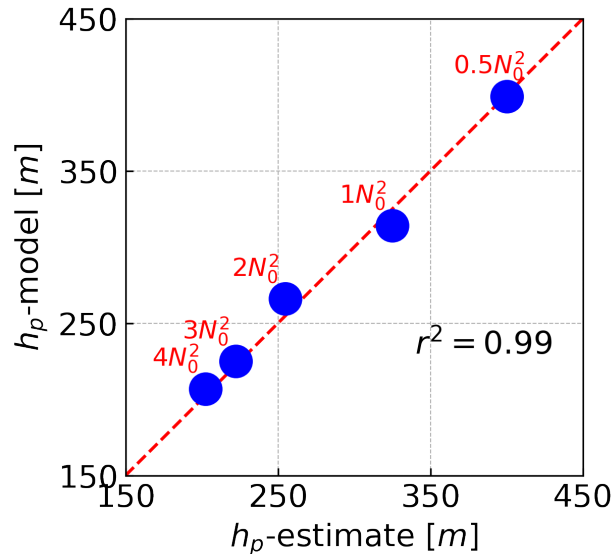
Figure 7. A comparison between the plume height estimated from theory and from the model. The fjord depth is $400\ m$, and an empirical coefficient of $h_0 = 1.69$ is used.

does result in significant cooling of the lower layer. A buoyant plume formed by injection of freshwater at depth and rising through a stratified fluid can result in the plume reaching neutral buoyancy well below the surface. Because this reduces the height from the bottom at which the plume detaches from the glacier, it also impacts the overall entrainment of warm ambient water and resulting submarine melting driven by the ascending plume. In this section we focus on how these subsurface plumes interact with a shallow sill.

A scaling for the height h_p that a plume generated by a point source of subglacial discharge reaches can be estimated from (Slater et al., 2016):

$$h_p = h_0(N_0^2)^{-3/8}\left(\frac{g_0' Q_{sg}}{2\pi\gamma^2}\right)^{1/4} \tag{6}$$

Based on buoyant plume theory (Morton et al., 1956), the terminal depth depends on the reduced gravity of the plume g_0' evaluated at the grounding line with the fresh plume density and a Boussinesq reference density, the entrainment coefficient γ, here taken to be 0.1, and the ambient stratification N_0^2. h_0 is a non-dimensional height that is related to the radius, velocity and reduced gravity of the plume. We tested this scaling with our model with a set of runs with a constant subglacial discharge of $250\ m^3\,s^{-1}$ and constant stratification N_0^2. Initial temperature is set to $10\ ^\circ C$ and the initial salinity is set to increase linearly from the surface to the bottom with ranges that represent weakly- to strongly-stratified glacial fjords. While highly simplified, these initial profiles provide a sensible set of runs to compare against the theory.

With an empirical coefficient of $h_0 = 1.69$, Eq. (6) predicted the height of the plume outflow well across a range of initial stratification conditions (Fig. 7). A surface plume outflow at the beginning of the simulation is observed in the least-stratified
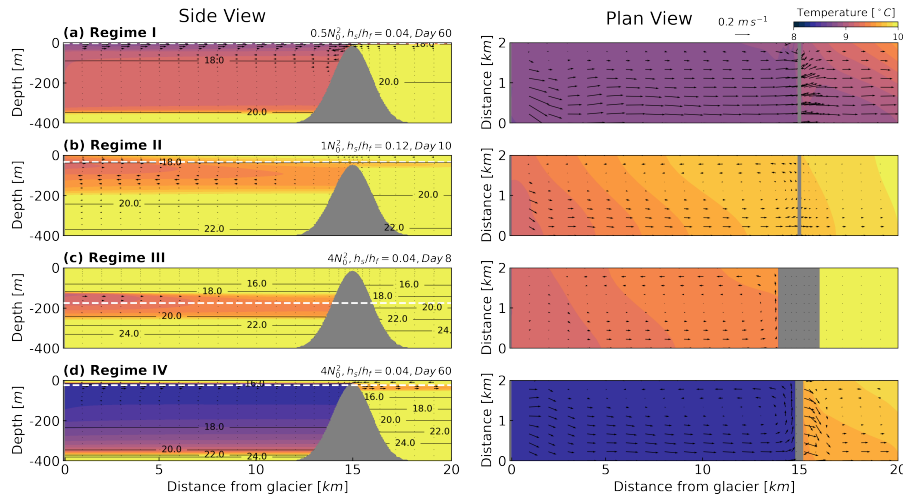
Figure 8. Snapshots of fjord circulation regimes from side (left panel) and plan (right panel) views. Black contours denote water density anomaly, white dashed lines indicate the depths at which the plan-view snapshots are taken, grey shaded areas represent sill locations. Across-fjord structures of the regimes can be found in Fig. S1 and Fig. S2.

case ($0.5N_0^2$). As expected, the higher stratification cases lead to plumes entering the fjord increasingly deeper, with values ranging from 0 to $\sim 200\ m$.

The relative depth of the fjord h_f, the sill h_s, and the height of the plume h_p help define circulation regimes that were

275   evident in our model outputs. When the stratification is weak or the subglacial discharge relatively strong so that $h_p/h_f \geq 1$, the circulation is characterized by the near steady, two-layer exchange flow that we described in the base case, where hydraulic control and the rate of reflux of the cold, outgoing plume water into the lower layer are the dominant processes controlling the cooling of the lower layer temperature (Fig. 8a). When $h_p/h_f < 1$ (i.e., a subsurface plume) and $h_p/(h_f - h_s) > 1$ (i.e., the plume depth is above the sill) a three-layer circulation regime is formed, with a subsurface freshwater overlying oceanic

280   inflow into the fjord (Fig. 8b). In our runs, the surface layer above the outgoing plume showed a rather weak circulation, and was largely transitory as the outgoing plume continued to mix and eventually reached the surface. However, this relatively fast transition might not be generally the case in fjords with deeper sills, relatively weak subglacial discharge, or relatively strong stratification.

The circulation regimes that lead to the strongest deep cooling are associated with $h_p/(h_f - h_s) \leq 1$. In those cases, the

285   freshwater plume is unable to exit the fjord, at least initially. The first circulation regime shows the outgoing plume reaching the sill and forming an horizontal recirculation. Heat being drawn from the deep fjord waters cannot be replaced with exchange with the shelf, and thus the deep fjord continues to cool as the heat budget is fundamentally unsteady. The subsurface (and sub-sill) plume continues to mix with the surrounding waters, rising in the process (Fig. 8c). While not all of our $h_p/(h_f - h_s) < 1$ cases reached this state in our 60-day runs, some did show the plume eventually reaching the sill depth, allowing the plume

290   to exit the fjord and thus forming a last distinct circulation regime. In this configuration, the circulation resembles a reverse
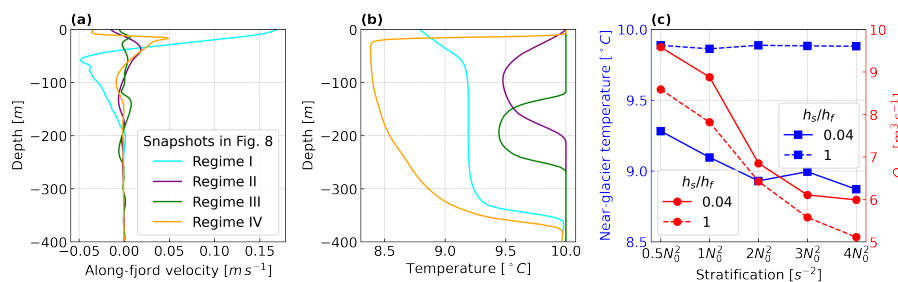
Figure 9. The along-fjord velocity (a), temperature (b) profiles corresponding to Regime I-IV, and the impact of shallow sill vs. fjord stratification on near-glacier temperature and submarine melting. Vertical profiles in (a) and (b) are collected at section S1, results in (c) are averaged over the last 14 days of the simulation.

estuary, where exchange is either lateral or vertical (Fig. 8d), but outflow is concentrated just above the sill. However, this regime is also fundamentally unsteady because heat entrained into the outgoing plume from the deep water in the fjord cannot be readily replaced with exchange with the shelf, leading to continuous cooling of that layer.

In summary, we find that for cases where the circulation regime is dominated by a two or three layer exchange flow at
295   the sill with inflow from the ocean at depth, the dynamics of mixing and reflux discussed in the base case are critical to understanding how deep fjord properties will evolve. In these cases, a steady view of the circulation in at least seasonal time scales is reasonable, as heat exchange at the mouth of the fjord can compensate for the heat loss due to mixing and melting. But when either strong stratification or weak subglacial discharge leads to a deep (relative to the sill) outflowing plume, cooling of the deep fjord is not caused by reflux but rather mixing of warm water into the plume which cannot be replaced by exchange
300   with the shelf. Critically, this means that the properties in the fjord are strongly time dependent, and sill processes become less important.

The regimes are defined from the interaction between stratification and the sill, thereby the variations in fjord stratification and sill depth may have major impacts on the circulation structure, heat transport pattern, and therefore melting at the glacier front. Figure 9a, b show the vertical profiles of along-fjord velocity and temperature inside the fjord corresponding to the
305   four distinct regimes, which are identified at different time with varied stratification and sill depth. As water properties and stratification change over time, the fjord circulation may fit into diverse regimes from the beginning to the end of simulations. Consistent with the effect of sill-driven reflux and heat transport regimes, water column temperature near the glacier front indicate a fjord cooling caused by a shallow sill and stronger initial stratification (Fig. 9c). In addition, the relative impact between stratification and the shallow sill on submarine melting showed that the reflux driven by a shallow sill increased
310   the melting compared to all the no-sill cases (Fig. 9c). To understand this counter-intuitive effect from sill-driven reflux, the variation of submarine melting, near-glacier temperature and stratification are presented in Fig. 10. Except at the very beginning of simulation with the shallowest sill, both cases coincide with Regime I, where the plume drives a surface outflow. When there is no sill ($h_s/h_f = 1$), the melting, fjord temperature, and stratification remained stable throughout the entire simulation (Fig. 10b, d, f). With the presence of a shallow sill ($h_s/h_f = 0.04$), however, submarine melting became higher especially after
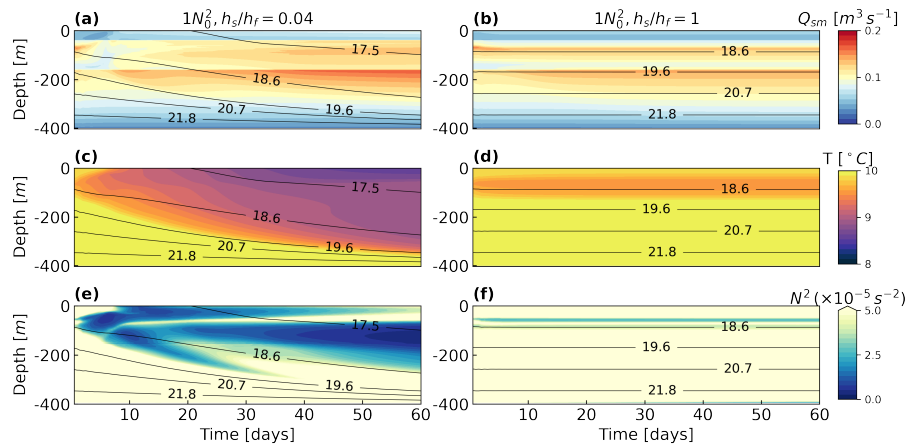
Figure 10. The evolution of submarine melting (a, b), near-glacier temperature (c, d), and near-glacier stratification (e, f) with (left panel) and without (right panel) a sill. Both cases have the same initial stratification ($1N_0^2$) and mostly fit in Regime I.

around 30 days (Fig. 10a). During that period, the fjord temperature dropped continuously as expected from the cooling effect of sill-driven reflux (Fig. 10c). Meanwhile, the fjord stratification became significantly weaker due to the strong mixing with the refluxed plume outflow (Fig. 10e). The fjord cooling and the decreased stratification both induced by sill-driven reflux have opposite impacts on glacial melt, and in our cases here the effect from stratification is more pronounced than that from fjord temperature, resulting in less heat supply to the glacier but increased submarine melting.

In general, the sill-driven reflux and the heat supply towards glaciers are impacted in different circulation regimes. With a surface or subsurface outflow in Regime I and II (Fig. 11a, b), the plume water being refluxed is modulated by the sill depth and subglacial discharge, and it cools the deep fjord by drawing down significant amount of cold water. When the discharge is weak or the ambient stratification is strong, the plume enters the fjord at a height below the sill, in which case the reflux is barely generated while the plume-driven outflow fills and cools the fjord basin progressively (Fig. 11c). As mixing continues and the plume rises to a higher level right above the sill, the circulation pattern in Regime IV (Fig. 11d) can also be viewed as a transition period from Regime III to Regime II and I. Based on our simulations, the unsteady scenario of Regime IV may last at least for a seasonal timescale, the deep fjord is continuously cooled by the mixing with outgoing plume and the sill-driven reflux.

3.3 The Impact of Tides

Tides are another important process that modulates the inflow of warm shelf waters in fjords and promotes turbulence and mixing. In a non-dimensional format, we use the ratio of the maximum tidal current amplitude U_t to the exchange flow velocity U_e at the sill to illustrate the strength of tidal forcing. U_t is obtained at the sill using tidal harmonic analysis. U_e is scaled by
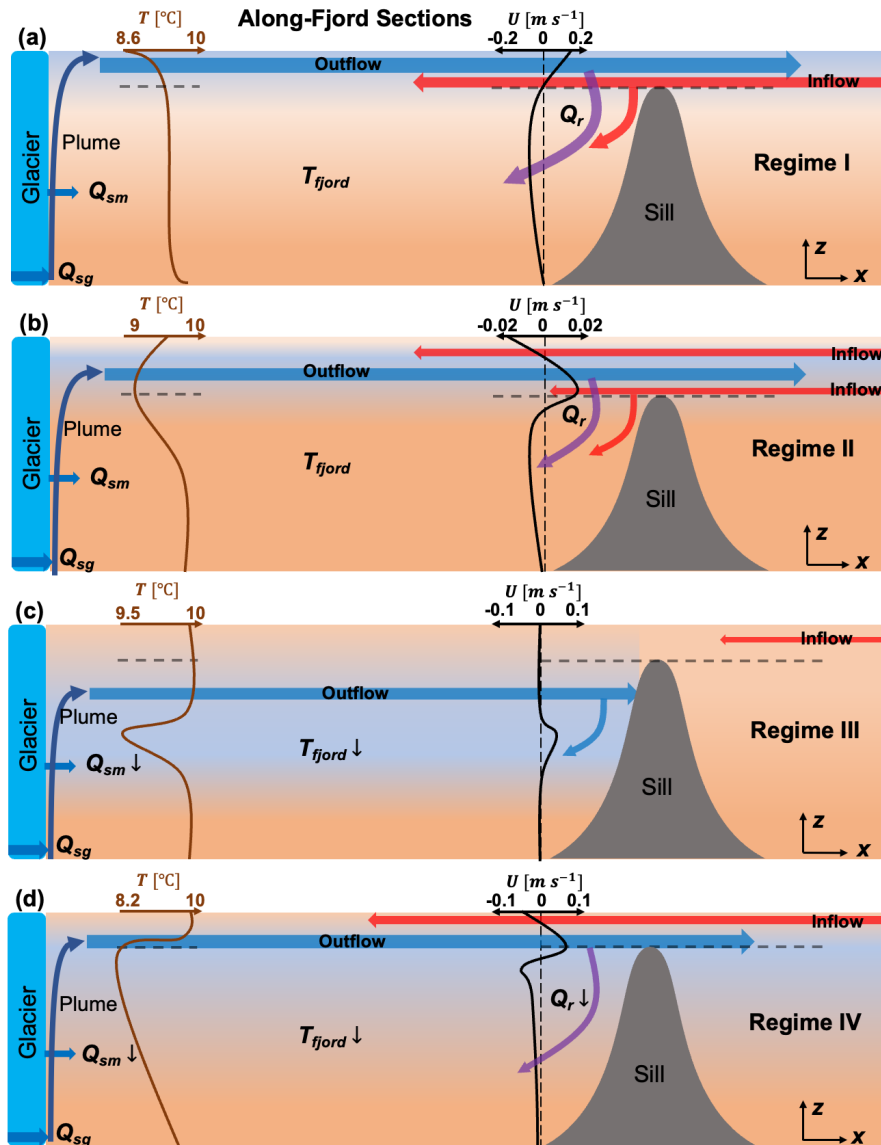
Figure 11. Schematics of fjord structure and circulation for different regimes. Brown and black curves are approximate temperature profiles near the glacier front and along-fjord velocity profiles on the glacierward side of the sill respectively. Horizontal dashed grey lines indicate the maximum sill height. Colors of shades and arrows represent relative water temperatures. Sizes of arrows indicate the relative magnitude of transports. Parameters depicted include subglacial discharge (Q_{sg}), submarine melting (Q_{sm}), deep-fjord temperature (T_s), and sill-driven reflux (Q_r).

$$U_e = \frac{Q_e}{A_{sill}/2} \tag{7}$$

Table 4. Tidal-exchange velocity ratio (U_t/U_e), outflow volume transport at S1 (Q_1^{out}), downward reflux fraction (α_{11}), downward reflux over sill (Q_r), fjord-shelf temperature ratio (T_{fjord}/T_{shelf}), submarine melting (Q_{sm}), mean stratification (N^2) near the glacier front for tidal experiments with $h_s/h_f = 0.04$.

U_t/U_e	Q_1^{out} $(m^3\,s^{-1})$	α_{11} (%)	Q_r $(m^3\,s^{-1})$	T_{fjord}/T_{shelf} (%)	Q_{sm} $(m^3\,s^{-1})$	N^2 $(\times 10^{-5}s^{-2})$
0	9025	71.5	6352	95.9	9.9	7
0.7	9006	70.3	6330	95.9	10.5	7
1.3	9018	67.7	6104	95.9	10.5	7
1.6	9626	58.1	5595	95.9	10.5	7
1.9	10389	46.7	4852	95.8	10.6	6.94
6.5	24877	21.0	5229	95.8	12.9	5.55

where Q_e is the exchange flow transport defined as $(Q_{out} + Q_{in})/2$ (Q_{in}, Q_{out} are positive) and A_{sill} is the cross-channel area at the sill crest. In the tidal simulations, U_t ranges between 0.1 to 1 $m\,s^{-1}$ and U_e has little variation, ranging between 0.13 to 0.15 $m\,s^{-1}$. With the shallowest sill ($h_s/h_f = 0.04$), the exchange in the fjord, sill-driven reflux, deep fjord temperature, and submarine melting before and after the tidal forcing is applied are summarized in Table 4.

With higher tidal velocity, the along-fjord exchange (Q_e) is enhanced by the flood and ebb tides as expected. In contrast, the downward reflux fraction (α_{11}) decreased significantly with stronger tidal forcing as the tidal velocity surpassing the exchange velocity ($U_t/U_e > 1$). In most cases, the reflux volume at the sill (Q_r) also decreased with stronger tides, as a result of increased exchange flow but more reduced reflux fractions. As for the deep-fjord temperature, it remained more or less the same since the magnitude of water exchange did not change much across all these runs. Still, submarine melting Q_{sm} increased by 6% to 30% when the barotropic tides are introduced, probably due to other heat sources to the near-glacier region brought by tidal currents (e.g., Mortensen et al., 2011). Additionally, the ambient stratification was weakened by strong tides, contributing to higher glacial melt. Because the results are derived at the steady state after tidally averaging, tidal effects are likely to be smoothed and Q_{sm} stayed unchanged with higher tidal amplitudes. In general, tidal forcing acts to intensify both the horizontal and vertical exchanges, modifying the composition of fjord waters. However, it has much less pronounced impact on the sill-driven reflux and the heat supply towards glaciers in such a shallow-silled fjord compared to other parameters.

4 Discussion

4.1 Application to Realistic Fjord Systems

The sill reflux process discussed above has been discussed in observational studies in both non-glacial and glacial fjords. In Loch Sunart, a shallow-silled Scottish fjord, hydrographic and current meter data collected during the summers of 1987, 1989, and 1990 revealed that an estimated 20% to 70% of the surface water recirculated into the bottom layer (Gillibrand et al., 1995). At Godthåbsfjord, Greenland, the summer surface water in the sill region was observed to reach the glacier terminus

355   at depth, with the subsurface freshwater fraction increasing from the winter (3%) to summer (10%) (Mortensen et al., 2013). The results highlighted mixing process at the sill that resembles the reflux of glacial freshwater we are focusing on here. Most recently, observations in LeConte Bay, Alaska ($h_s/h_f = 0.06$) showed that 50% to 75% of the summer inflow was composed of refluxed plume-driven outflow (Hager et al., 2022). This range is comparable to our base case simulations (Fig. 5b).

      The circulation regimes identified here (Fig. 11) suggest that conceptual models of glacier melting where the circulation and
360   heat budget of the fjord are steady might not be adequate. When the plume flow away from the glacier is either blocked by the sill or just above sill level, replacing the heat used for deep melting with deep waters outside of the fjord becomes difficult. During the summer, glacial fjords in Greenland (Mortensen et al., 2013), Alaska (Hager et al., 2022) and Patagonia (Moffat et al., 2018) show intense subglacial discharge and surface or subsurface plume outflow and exhibiting circulation patterns in Regime I and Regime II (Fig. 11a, b). With stronger ambient stratification or weaker winter subglacial discharge , buoyant
365   plumes enter the fjord at depth, forming an outflow that intersects the sill or mostly blocked by it (Gladish et al., 2015; Carroll et al., 2016), resembling Regime III (Fig. 11c), in which case the blocked outflowing plume is expected to progressively cool the deep fjord. We were not able to find published reports of Regime IV (Fig. 11d), a kind of reverse estuary circulation (e.g., Giddings and MacCready, 2017), perhaps because this circulation could quickly transition to Regime II or I. Because Regime III and IV reflect an unsteady state for the heat budget for the fjord, and the melting rate depends on the resulting deep fjord
370   temperature, caution should be used when applying a melting parameterization that assumes a steady circulation in the ocean.

      Our simplified model configuration necessarily removes what possibly be key processes modulating both the reflux process and its impact on the heat supply to the ice. While we explored tidal variability briefly, the reason for the reduction of the reflux under stronger tidal currents, also reported by Hager et al. (2022), is not well understood, and will be explored in a future study. Wind forcing is a well known factor influencing exchange between proglacial fjords and the open ocean (Straneo et al.,
375   2010; Jackson et al., 2014; Moffat, 2014). Finally, we did not fully explore how more realistic sill depths, multiple sills, or different fjord widths might influenced the processes here. However, we believe the regimes discussed above still provide a useful framework to move forward.

4.2 Implications for Glacial Melt

      Our results show that the downward transport of outflowing glacial freshwater at the sill cools the fjord, which is not entirely
380   surprising. Although the sill-fjord depth ratio h_s/h_f has a significant impact on the downward reflux fraction (Fig. 5b), the magnitude of reflux and thus the warm water supply towards glaciers are largely determined by the strength of subglacial discharge, especially with a shallower sill. Depending on properties of the outflow, the sill-driven reflux may have either reduce or increase heat transport to the glacier. For example, numerical experiments by Hager et al. (2022) found that the warmest surface water during the summer was refluxed and transported to LeConte Glacier terminus, enhancing heat supply
385   and submarine melting. In contrast, our results show the heat flux towards the glacier near the glacier front (H_f^0) only has slight variation with different sill depths (Table 2), because the reflux of cold outflow cools shelf water as they cross the sill, but the circulation remains intense in the fjord.

In our simulations, the presence of the sill generates several circulation regimes, two of which have been observed in several systems (I and II), and another for which some evidence exists (IV). In the former, the reflux process leads to a decrease in both temperature and stratification of the deep inflow, which has competing effects on the submarine melting. In our simulations, the stratification effect generally overcame the cooling, leading to higher submarine melting for the shallow sill cases. However, several caveats should be considered: first, depending on the shelf water structure outside the fjord, a shallow sill might favor overall warmer waters entering the fjord, as it happens in Jorge Montt glacier. More critically, glacial melt away from discrete subglacial discharge outlets freshens the adjacent fjord water and drives weak buoyant plumes (Magorrian and Wells, 2016). This ambient melting considered to be negligible in our model, but has been shown to be a significant part of the total submarine meltwater flux in real systems (Jackson et al., 2020). These background melt plumes also entrain fjord waters and intrude into the fjord after reaching neutral buoyancy. However, it is unclear whether systems where background melting dominates the freshwater output can be conceptualized using discrete plumes as we did here. Additionally, coefficients used in submarine melt parameterization are derived from ice shelf studies (Cowton et al., 2015), hence the dynamics and morphology in the near-ice zone might be substantially different at tidewater glaciers (Jackson et al., 2022). Point-source representation of plume geometry is likely to underestimate entrainment and plume-drive melt, according to measurements of near-glacier circulation (Jackson et al., 2017). As a result, models like we use here are likely to generate submarine melt rates that are far too low in most cases.

Despite these important caveats, the fundamental dynamics that lead to retention of meltwater and resulting unsteady state budgets in shallow-silled fjords, the competing effects of cooling and destruction of stratification of the sill on melting rates, and the importance of reflux processes are the sill are likely to be at play in real systems or improved models that include background melting and other important corrections.

5 Conclusions

Mixing and advection processes on shallow sills separating glacial fjords from the open ocean play a critical role in modulating the circulation and heat supply to marine-terminating glaciers. Using a coupled plume-ocean fjord model, we find four circulation regimes that depend on the ratios of the sill depth h_s, the fjord depth h_f and the depth of the meltwater plume depth h_p. In the first two regimes, the outgoing meltwater plume flows above the sill, either at the surface (I) or below it (II), resembling a more typical (i.e., non-glacial), steady fjord exchange, where the heat lost to ice melting can be replaced by oceanic sources. In the other two regimes, however, the plume is either trapped within the fjord by the sill (III) or exits just above it (IV). In either case, the deep fjord layer continues to lose heat as exchange with the open ocean is blocked. In our 60-day simulations, these unsteady state conditions can last for the entire run, suggesting that even in seasonal time scales the assumption that a marine-terminating glacier will respond to changes in shelf conditions might be flawed, at least in some cases.

In the regimes where a steady state solution is possible (I and II) and the meltwater plume exits the fjord, strong vertical exchange (reflux) is induced over the sill. The exchange is dominated by downward transport of cold outflow from the upper layer to the warm inflowing water from the ocean, thus contributing to a significant recirculation within the fjord. With a sill

depth of $h_s/h_f = 0.04$, about 70% of the plume-driven outflow is refluxed to depth. A range of simulations show that the fraction of the outflow being refluxed is partially controlled by the sill-fjord maximum depth ratio h_s/h_f, and that increasing the subglacial discharge, and hence the outgoing meltwater outflow from the fjord, increases the reflux as well. Critically, we find that the sill processes in those circulation regimes result in a decrease of both deep fjord temperature and stratification, which have opposite effects in the melting rate of the glacier. In our simulations, the stratification effect tended to dominate, resulting in higher melting even though the incoming ocean water was cooled at the sill. However, recent observational studies (Jackson et al., 2020, 2022) suggest caution in evaluating the overall magnitude of melting we see in our simulations as key processes, including background melting away from regions of subglacial melting input not represented in our model, might have a much larger role than previously thought. However, the generation of the circulation regimes we discuss here are more strongly tied to the formation of subsurface (including below the sill depth) meltwater plumes, regardless of what fraction of that meltwater is of subglacial origin or melted locally.

Overall, our simulations show that vertical exchange at the sill significantly modulates heat supply to tidewater glaciers terminated in shallow-silled fjords, through the sill-driven reflux of glacial freshwater. The relative depth of the plume outflow, the fjord, and the sill provides a useful framework to characterize the circulation and heat transport patterns in glacial fjords.

Data availability. The IcePlume package (Cowton et al., 2015) of MITgcm can be accessed through https://github.com/tcowton/iceplume. Model output and code used in the analysis is available from the authors upon request (wbao@udel.edu).

Author contributions. W.B. wrote the manuscript and made the data analysis with constant advice, suggestions and corrections by C.M..

Competing interests. The contact author has declared that neither of the authors has any competing interests.

Acknowledgements. W.B. was supported by a fellowship from the School of Marine Sciences and Policy, University of Delaware. C.M. received support from COPAS Coastal (ANID FB210021) program. Both authors were supported by University of Delaware Research Foundation Grant #18A00956. We thank Dustin Carroll for his help setting up the IcePlume model. This research was supported in part through the use of Information Technologies (IT) resources at the University of Delaware, specifically the high-performance computing resources.

References

445   Arneborg, L., Erlandsson, C. P., Liljebladh, B., and Stigebrandt, A.: The rate of inflow and mixing during deep-water renewal in a sill fjord, Limnology and Oceanography, 49, 768–777, https://doi.org/10.4319/lo.2004.49.3.0768, 2004.

Bartholomaus, T. C., Stearns, L. A., Sutherland, D. A., Shroyer, E. L., Nash, J. D., Walker, R. T., Catania, G., Felikson, D., Carroll, D., and Fried, M. J.: Contrasts in the response of adjacent fjords and glaciers to ice-sheet surface melt in West Greenland, Annals of Glaciology, 57, 25–38, 2016.

450   Carroll, D., Sutherland, D. A., Hudson, B., Moon, T., Catania, G. A., Shroyer, E. L., Nash, J. D., Bartholomaus, T. C., Felikson, D., Stearns, L. A., Noël, B. P. Y., and van den Broeke, M. R.: The impact of glacier geometry on meltwater plume structure and submarine melt in Greenland fjords, Geophysical Research Letters, 43, 9739–9748, https://doi.org/10.1002/2016GL070170, 2016.

Carroll, D., Sutherland, D. A., Shroyer, E. L., Nash, J. D., Catania, G. A., and Stearns, L. A.: Subglacial discharge-driven renewal of tidewater glacier fjords, Journal of Geophysical Research: Oceans, 122, 6611–6629, 2017.

455   Cokelet, E. D. and Stewart, R. J.: The exchange of water in fjords: The efflux/reflux theory of advective reaches separated by mixing zones, Journal of Geophysical Research: Oceans, 90, 7287–7306, 1985.

Cowton, T., Slater, D., Sole, A., Goldberg, D., and Nienow, P.: Modeling the impact of glacial runoff on fjord circulation and submarine melt rate using a new subgrid-scale parameterization for glacial plumes, Journal of Geophysical Research: Oceans, 120, 796–812, 2015.

Geyer, W. R. and Cannon, G. A.: Sill processes related to deep water renewal in a fjord, Journal of Geophysical Research: Oceans, 87, 460   7985–7996, 1982.

Geyer, W. R. and MacCready, P.: The Estuarine Circulation, Annual Review of Fluid Mechanics, 46, 175–197, https://doi.org/10.1146/annurev-fluid-010313-141302, 2014.

Giddings, S. N. and MacCready, P.: Reverse Estuarine Circulation Due to Local and Remote Wind Forcing, Enhanced by the Presence of Along-Coast Estuaries, Journal of Geophysical Research: Oceans, 122, 10 184–10 205, https://doi.org/10.1002/2016JC012479, 2017.

465   Gillibrand, P. A., Turrell, W. R., and Elliott, A. J.: Deep-Water Renewal in the Upper Basin of Loch Sunart, a Scottish Fjord, Journal of Physical Oceanography, 25, 1488–1503, https://doi.org/10.1175/1520-0485(1995)025<1488:DWRITU>2.0.CO;2, 1995.

Gladish, C. V., Holland, D. M., Rosing-Asvid, A., Behrens, J. W., and Boje, J.: Oceanic Boundary Conditions for Jakobshavn Glacier. Part I: Variability and Renewal of Ilulissat Icefjord Waters, 2001–14, Journal of Physical Oceanography, 45, 3–32, https://doi.org/10.1175/JPO-D-14-0044.1, 2015.

470   Hager, A. O., Sutherland, D. A., Amundson, J. M., Jackson, R. H., Kienholz, C., Motyka, R. J., and Nash, J. D.: Subglacial Discharge Reflux and Buoyancy Forcing Drive Seasonality in a Silled Glacial Fjord, Journal of Geophysical Research: Oceans, 127, e2021JC018 355, https://doi.org/10.1029/2021JC018355, 2022.

Holland, D. M. and Jenkins, A.: Modeling Thermodynamic Ice–Ocean Interactions at the Base of an Ice Shelf, Journal of Physical Oceanography, 29, 1787–1800, https://doi.org/10.1175/1520-0485(1999)029<1787:MTIOIA>2.0.CO;2, 1999.

475   Hugonnet, R., McNabb, R., Berthier, E., Menounos, B., Nuth, C., Girod, L., Farinotti, D., Huss, M., Dussaillant, I., Brun, F., and Kääb, A.: Accelerated global glacier mass loss in the early twenty-first century, Nature, 592, 726–731, https://doi.org/10.1038/s41586-021-03436-z, 2021.

Inall, M., Cottier, F., Griffiths, C., and Rippeth, T.: Sill dynamics and energy transformation in a jet fjord, Ocean Dynamics, 54, 307–314, 2004.

480   Jackson, R. H. and Straneo, F.: Heat, Salt, and Freshwater Budgets for a Glacial Fjord in Greenland, Journal of Physical Oceanography, 46,
       2735–2768, https://doi.org/10.1175/JPO-D-15-0134.1, 2016.

       Jackson, R. H., Straneo, F., and Sutherland, D. A.: Externally forced fluctuations in ocean temperature at Greenland glaciers in non-summer
       months, Nature Geoscience, 7, 503–508, https://doi.org/10.1038/ngeo2186, 2014.

       Jackson, R. H., Shroyer, E. L., Nash, J. D., Sutherland, D. A., Carroll, D., Fried, M. J., Catania, G. A., Bartholomaus, T. C., and Stearns, L. A.:
485   Near-glacier surveying of a subglacial discharge plume: Implications for plume parameterizations: SUBGLACIAL PLUME STRUCTURE
       AND TRANSPORT, Geophysical Research Letters, 44, 6886–6894, https://doi.org/10.1002/2017GL073602, 2017.

       Jackson, R. H., Nash, J. D., Kienholz, C., Sutherland, D. A., Amundson, J. M., Motyka, R. J., Winters, D., Skyllingstad, E., and Pettit,
       E. C.: Meltwater Intrusions Reveal Mechanisms for Rapid Submarine Melt at a Tidewater Glacier, Geophysical Research Letters, 47,
       e2019GL085 335, https://doi.org/10.1029/2019GL085335, 2020.

490   Jackson, R. H., Motyka, R. J., Amundson, J. M., Abib, N., Sutherland, D. A., Nash, J. D., and Kienholz, C.: The Relationship Between
       Submarine Melt and Subglacial Discharge From Observations at a Tidewater Glacier, Journal of Geophysical Research: Oceans, 127,
       e2021JC018 204, https://doi.org/10.1029/2021JC018204, 2022.

       Kimura, S., Holland, P. R., Jenkins, A., and Piggott, M.: The Effect of Meltwater Plumes on the Melting of a Vertical Glacier Face, Journal
       of Physical Oceanography, 44, 3099–3117, https://doi.org/10.1175/JPO-D-13-0219.1, 2014.

495   Large, W. G., McWilliams, J. C., and Doney, S. C.: Oceanic vertical mixing: A review and a model with a nonlocal boundary layer parame-
       terization, Reviews of Geophysics, 32, 363–403, https://doi.org/10.1029/94RG01872, 1994.

       Losch, M.: Modeling ice shelf cavities in az coordinate ocean general circulation model, Journal of Geophysical Research: Oceans, 113,
       2008.

       Love, K. B., Hallet, B., Pratt, T. L., and O'neel, S.: Observations and modeling of fjord sedimentation during the 30 year retreat of Columbia
500   Glacier, AK, Journal of Glaciology, 62, 778–793, https://doi.org/10.1017/jog.2016.67, 2016.

       MacCready, P.: Calculating Estuarine Exchange Flow Using Isohaline Coordinates, Journal of Physical Oceanography, 41, 1116–1124,
       https://doi.org/10.1175/2011JPO4517.1, 2011.

       MacCready, P., Geyer, W. R., and Burchard, H.: Estuarine exchange flow is related to mixing through the salinity variance budget, Journal of
       Physical Oceanography, 48, 1375–1384, 2018.

505   MacCready, P., McCabe, R. M., Siedlecki, S. A., Lorenz, M., Giddings, S. N., Bos, J., Albertson, S., Banas, N. S., and Garnier, S.: Es-
       tuarine Circulation, Mixing, and Residence Times in the Salish Sea, Journal of Geophysical Research: Oceans, 126, e2020JC016 738,
       https://doi.org/https://doi.org/10.1029/2020JC016738, 2021.

       Magorrian, S. J. and Wells, A. J.: Turbulent plumes from a glacier terminus melting in a stratified ocean, Journal of Geophysical Research:
       Oceans, 121, 4670–4696, https://doi.org/10.1002/2015JC011160, 2016.

510   Marshall, J., Adcroft, A., Hill, C., Perelman, L., and Heisey, C.: A finite-volume, incompressible Navier Stokes model for studies of the
       ocean on parallel computers, Journal of Geophysical Research: Oceans, 102, 5753–5766, 1997.

       Moffat, C.: Wind-driven modulation of warm water supply to a proglacial fjord, Jorge Montt Glacier, Patagonia, Geophysical Research
       Letters, 41, 3943–3950, 2014.

       Moffat, C., Tapia, F. J., Nittrouer, C. A., Hallet, B., Bown, F., Boldt Love, K., and Iturra, C.: Seasonal evolution of ocean heat supply and
515   freshwater discharge from a rapidly retreating tidewater glacier: Jorge Montt, Patagonia, Journal of Geophysical Research: Oceans, 123,
       4200–4223, 2018.

Mortensen, J., Lennert, K., Bendtsen, J., and Rysgaard, S.: Heat sources for glacial melt in a sub-Arctic fjord (Godthåbsfjord) in contact with the Greenland Ice Sheet, Journal of Geophysical Research: Oceans, 116, https://doi.org/10.1029/2010JC006528, 2011.

Mortensen, J., Bendtsen, J., Motyka, R. J., Lennert, K., Truffer, M., Fahnestock, M., and Rysgaard, S.: On the seasonal freshwater stratifi-
cation in the proximity of fast-flowing tidewater outlet glaciers in a sub-Arctic sill fjord, Journal of Geophysical Research: Oceans, 118, 1382–1395, https://doi.org/10.1002/jgrc.20134, 2013.

Morton, B. R., Taylor, G. I., and Turner, J. S.: Turbulent gravitational convection from maintained and instantaneous sources, Proceedings of the Royal Society of London. Series A. Mathematical and Physical Sciences, 234, 1–23, https://doi.org/10.1098/rspa.1956.0011, 1956.

Motyka, R. J., Dryer, W. P., Amundson, J., Truffer, M., and Fahnestock, M.: Rapid submarine melting driven by subglacial discharge, LeConte Glacier, Alaska, Geophysical Research Letters, 40, 5153–5158, 2013.

Rayson, M. D., Gross, E. S., Hetland, R. D., and Fringer, O. B.: Time scales in Galveston Bay: An unsteady estuary, Journal of Geophysical Research: Oceans, 121, 2268–2285, https://doi.org/https://doi.org/10.1002/2015JC011181, 2016.

Rignot, E., Fenty, I., Xu, Y., Cai, C., Velicogna, I., Cofaigh, C., Dowdeswell, J. A., Weinrebe, W., Catania, G., and Duncan, D.: Bathymetry data reveal glaciers vulnerable to ice-ocean interaction in Uummannaq and Vaigat glacial fjords, west Greenland, Geophysical Research Letters, 43, 2667–2674, 2016.

Schaffer, J., Kanzow, T., von Appen, W.-J., von Albedyll, L., Arndt, J. E., and Roberts, D. H.: Bathymetry constrains ocean heat supply to Greenland's largest glacier tongue, Nature Geoscience, 13, 227–231, https://doi.org/10.1038/s41561-019-0529-x, 2020.

Sciascia, R., Cenedese, C., Nicolì, D., Heimbach, P., and Straneo, F.: Impact of periodic intermediary flows on submarine melting of a Greenland glacier, Journal of Geophysical Research: Oceans, 119, 7078–7098, https://doi.org/10.1002/2014JC009953, 2014.

Slater, D. A., Goldberg, D. N., Nienow, P. W., and Cowton, T. R.: Scalings for Submarine Melting at Tidewater Glaciers from Buoyant Plume Theory, Journal of Physical Oceanography, 46, 1839–1855, https://doi.org/10.1175/JPO-D-15-0132.1, 2016.

Straneo, F. and Cenedese, C.: The dynamics of Greenland's glacial fjords and their role in climate, Annual review of marine science, 7, 89–112, 2015.

Straneo, F., Hamilton, G. S., Sutherland, D. A., Stearns, L. A., Davidson, F., Hammill, M. O., Stenson, G. B., and Rosing-Asvid, A.: Rapid circulation of warm subtropical waters in a major glacial fjord in East Greenland, Nature Geoscience, 3, 182–186, https://doi.org/10.1038/ngeo764, 2010.

Sutherland, D. A., Straneo, F., and Pickart, R. S.: Characteristics and dynamics of two major Greenland glacial fjords, Journal of Geophysical Research: Oceans, 119, 3767–3791, https://doi.org/10.1002/2013JC009786, 2014.

Wang, T., Geyer, W. R., and MacCready, P.: Total Exchange Flow, Entrainment, and Diffusive Salt Flux in Estuaries, Journal of Physical Oceanography, 47, 1205–1220, https://doi.org/10.1175/JPO-D-16-0258.1, 2017.

Xu, Y., Rignot, E., Menemenlis, D., and Koppes, M.: Numerical experiments on subaqueous melting of Greenland tidewater glaciers in response to ocean warming and enhanced subglacial discharge, Annals of Glaciology, 53, 229–234, 2012.

Xu, Y., Rignot, E., Fenty, I., Menemenlis, D., and Flexas, M. M.: Subaqueous melting of Store Glacier, west Greenland from three-dimensional, high-resolution numerical modeling and ocean observations, Geophysical Research Letters, 40, 4648–4653, https://doi.org/https://doi.org/10.1002/grl.50825, 2013.

Zhao, K. X., Stewart, A. L., and McWilliams, J. C.: Geometric Constraints on Glacial Fjord–Shelf Exchange, Journal of Physical Oceanography, 51, 1223–1246, 2021.